David Bach, Bo C. Christiansen, Dieter Schild*, and Horst Geckeis

TEM study of Green Rust Sodium Sulphate (GR$_{Na,SO4}$) Interacted with Neptunyl Ions (NpO$_2{}^+$)

Abstract: Green rust (GR) as sodium sulphate form, $NaFe(II)_6Fe(III)_3(OH)_{18}(SO_4)_2 \cdot 12H_2O$, is reacted with an aqueous solution of neptunyl ions (NpO$_2{}^+$) and the resulting Np(IV) solid phase is investigated at a nanometer scale by different transmission electron microscopy (TEM) techniques, including high-resolution TEM (HRTEM), high-angle annular dark-field scanning TEM (HAADF-STEM), energy-dispersive X-ray spectroscopy (EDXS), and electron energy-loss spectroscopy (EELS). The aim of the analyses is to achieve insight into the potential immobilization mechanism for Np(V) in the context of safety assessment of a nuclear-waste repository. The neptunium is found to be immobilized at the edge of the green rust platelets, in a rim composed of nanocrystallites about 2–3.5 nm in size. The EELS results and more particularly the HRTEM findings are consistent with NpO$_2$ crystallizing in a fluorite-type structure. Furthermore, the Np-O$_{4,5}$ edges recorded by EELS at the Np(IV) phase are presented, expanding the EELS-data set currently available in the literature for Np.

Keywords: Green rust sodium sulphate, Neptunyl, Neptunium dioxide, Nuclear-waste repository, TEM, HRTEM, HAADF, EDXS, EELS, Np-O$_{4,5}$ edges.

---

*Corresponding Author: Dieter Schild, Institute for Nuclear Waste Disposal, Karlsruhe Institute of Technology, P.O. Box 3640, 76021 Karlsruhe, Germany, E-mail: dieter.schild@kit.edu
David Bach, Horst Geckeis: Institute for Nuclear Waste Disposal, Karlsruhe Institute of Technology, P.O. Box 3640, 76021 Karlsruhe, Germany
Bo C. Christiansen: Nano-Science Center, Department of Chemistry, University of Copenhagen, Universitetsparken 5, 2100 Copenhagen Ø, Denmark

1 Introduction

Nuclear waste will be disposed within steel canisters in deep underground repositories. To assess the long-term safety of the repository, all possible processes that might have an impact on the release and transport of radionuclides in the environment must be taken into account. Particularly, the possibility of water gaining access to the waste cannot be excluded. Indeed, water is a prevailing transport medium for contaminants – including radionuclides – in the environment [1]. Furthermore, the environmental fate of radionuclides is primarily controlled by their solubilities depending on oxidation states which strongly depend on their interaction with redox-active materials in the near- and far-field of the repository [1, 2].

The present study is more particularly focused on the fate of the actinide [237]Np. It is a minor component (about 0.05 wt %) of spent U-based nuclear fuel but has a long half-life, $T_{1/2} = 2.144 \times 10^6$ years, and its concentration will increase during the first 5000 years of disposal by α-decay of [241]Am ($T_{1/2} = 432.2$ years). Thus, it will be a contributor to the long-term radiotoxicity of the nuclear waste [2]. Furthermore, it is of primary environmental concern because of its high solubility in the pentavalent state [1]. Hence, when water has access to the waste, neptunium may become particularly mobile in the form of neptunyl ions Np(V)O$_2{}^+$. In contrast, Np(IV)-species are orders of magnitude less soluble and have a high tendency to form aqueous complexes [1, 2]. Finally, Np is taken as a representative of redox-sensitive waste-borne radionuclides, showing distinctly different chemical behaviour at different oxidation states.

Green rust (GR) belongs to a family of Fe(II)-Fe(III) layered double hydroxides which oxidize in the presence of oxidising agents. It crystallizes in thin hexagonal platelets consisting of the stacking of positively charged brucite-like layers of Fe(II),Fe(III)-hydroxide with anions (*e.g.* Cl$^-$, CO$_3{}^{2-}$, or SO$_4{}^{2-}$), sometimes also cations (*e.g.* Na$^+$), and water structurally arranged in the interlayers [*e.g.*, 3–6]. It may form in anoxic groundwater [7] and is likely to evolve as a product of steel-canister corrosion in a nuclear-waste repository following groundwater access. Indeed, the formation of GR has for instance been observed during the corrosion of zerovalent-iron reactive media [*e.g.*, 8–10]. Furthermore, several studies reported the ability of GR to reduce a variety of redox-sensitive species including Cr(VI), Tc(VII), Se(IV,VI), Hg(II), U(VI), and Np(V) [11–22]. Hence, owing to its strongly reducing properties, GR is a potential candidate for attenuating the migration of redox-sensitive radionuclides in the environment.

Transmission electron microscopy (TEM) is a unique and versatile characterization technique enabling structural and chemical analysis of materials at a nanometer scale [*e.g.*, 23]. Because green rust particles are quite thin (~ 40 nm thick or less for $GR_{Na,SO4}$ synthesized by Christiansen *et al.* [6], the platelets are by nature "electron transparent" in the electron microscope, and thus, are well suited for TEM investigations [*e.g.*, 4, 15, 19]. Furthermore, TEM has already been successfully employed to study the properties of a variety of actinide materials [*e.g.*, 24]. Particularly, O'Loughlin *et al.* [15] demonstrated by means of TEM that the reduction of uranyl (U^{VI}) by GR results in the formation of UO_2 crystalline nanoparticles.

Recently, Skovbjerg *et al.* [21] and Christiansen *et al.* [22] investigated the interaction of NpO_2^+ with green rust of sodium sulphate form ($GR_{Na,SO4}$) (the two papers partially report the same experiments). They showed that Np(V) is immobilized *via* reduction and formation of less soluble Np(IV)-species. The authors performed preliminary TEM investigations (conventional TEM imaging, EDXS), however with a limited resolution (*e.g.* no high resolution TEM). Their results showed that Np was enriched at the GR-edges but gave no direct experimental proof concerning the nature of the Np(IV) phase formed. Christiansen *et al.* [22] suggested that it is hydrated NpO_2. However, this conclusion was not based on experimental evidence but the authors drew it through discussion, notably by comparing their findings with those of O'Loughlin *et al.* [15] – who studied the interaction between uranyl and GR – and those of Neck *et al.* [25] – who studied the reduction of Np(V) in aqueous solutions. Skovbjerg *et al.* [21] hypothesized that the Np(IV) phase could be NpO_2 or a Np-substituted iron- (oxyhydr)oxide. Hence, further investigations are required to clearly determine the nature of the Np(IV)-phase formed, and thus to achieve a safer understanding of the Np-immobilization mechanisms.

The present study continues the work of Skovbjerg *et al.* [21] and Christiansen *et al.* [22] and $GR_{Na,SO4}$ reacted with NpO_2^+ is investigated using a high-resolution field-emission transmission electron microscope. In this study we focus on the fate of Np. The first aim is the determination at a nanometer scale of the location where Np is immobilized on the GR particles. The second aim is to gather more information about the Np(IV)-containing phase formed. For these purposes, several TEM techniques are employed, including high-resolution TEM (HRTEM), high-angle annular dark-field scanning TEM (HAADF-STEM), energy-dispersive X-ray spectroscopy (EDXS), and also electron energy-loss spectroscopy (EELS). Provided that appropriate reference data are available for materials of known phases, EELS is a powerful tool to analyze an unknown compound [*e.g.*, 26, 27]. The present work extends the scarce EELS-data set available up to now in the literature for the $Np-O_{4,5}$ edges.

2 Experimental details

2.1 Materials and specimen preparation

Two types of specimens are analyzed: $GR_{Na,SO4}$ standard alone (GR) and after reaction with $^{237}Np(V)$ (Np-GR). The $GR_{Na,SO4}$ standard, of nominal formula $NaFe(II)_6Fe(III)_3(OH)_{18}(SO_4)_2 \cdot 12H_2O$, was prepared inside an anoxic glove box from a solution of $FeSO_4 \cdot 7H_2O$ by adding NaOH to bring the Fe/OH ratio to 0.6. As pH increased $Fe(OH)_2$ precipitates. When pH reached 8.4, the suspension was oxidized by bubbling CO_2-free air. Yield of transformation to GR is found out optimum at the inflection point reached at $\approx$ pH8−8.4 and pe − 7 according to Christiansen *et al.* [6]. The green rust material were prepared > 48 h prior to the experiments and kept sealed and anoxic, Oswald ripening of the green rust [28] is thus not expected to influence the experiments. The reaction with Np(V) was also performed in an anoxic glove box by mixing 20 μL of a NpO_2^+ stock solution (~ 7.74 mM/L, preparation described by Christiansen *et al.* [22] with 80 μL of a GR slurry (5.5 g/L) resulting in 1.55 mM/L Np in total and a Np(V):GR molar ratio of about 1 : 2.3, which is the same as a Np(V) : Fe(II)$_{GR}$ molar ratio of approximately 7 : 100. After 10 min reaction, the Np concentration in the supernatant (pH ~ 8, pe ~ −6.7) was less than 1.7×10^{-8} M/L (detection limit of liquid scintillation counting) indicating that Np was removed from the solution. Furthermore, X-ray photoelectron spectroscopy (XPS) of the solid phase showed a reduction of Np(V) to Np(IV) [21, 22]. In the following, the green rust interacted with neptunyl ions is denominated by the acronym Np-GR.

Specimens were prepared for TEM analyses by depositing few-μL droplets of GR or Np-GR suspensions on copper TEM grids covered by holey carbon films. The specimens were rinsed by a couple of MilliQ-water droplets to remove the loosely bound particles, and let to dry at ambient temperature after the excess solution was removed by means of a paper tissue.

Some regions of the Np-GR specimens were contaminated by a Si-containing compound present on the TEM-specimen holder used to investigate the radioactive material. When necessary, this contamination was taken into consideration while analyzing the results. Contact to air

could not be avoided during the transfer of the specimens from the preparation glove box to the microscope. It is thus possible that some Fe(II) were oxidized in the green rust samples at this moment. This could also be the case for Np-GR samples. Np(IV) re-oxidation to Np(V) was, however, not observed. In addition, the high vacuum conditions in the specimen chamber of the transmission electron microscope (approximately 10^{-5} Pa) probably induced a dehydration of the (Np-GR). In spite of these possible transformations of the original specimens, the acronyms GR and Np-GR are used throughout this study to designate the investigated materials.

2.2 Transmission electron microscopy (TEM)

The specimens were analyzed using a high-resolution *FEI Tecnai G^2 F20 X-Twin* transmission electron microscope located in a radioactive control area at the *Fusion Materials Laboratory* (IAM-WBM-FML) of the *KIT*. The instrument is equipped with a field emission gun and operates at 200 kV with a point resolution of 0.25 nm. It allows high-resolution TEM (HRTEM), can be operated in the scanning TEM (STEM) mode, and is equipped with a high-angle annular dark-field (HAADF) detector (*Fischione*), and an energy-dispersive X-ray spectroscopy (EDXS) system (*EDAX*). In addition, a post-column *Gatan imaging filter* (GIF) *Tridiem* allows electron energy-loss spectroscopy (EELS) as well as recording of images by a 2 k x 2 k *UltraScan* CCD camera. The acquisition and post-acquisition treatments of images and spectra were performed with the *Gatan Digital Micrograph* or *TEM Imaging and Analysis* (*FEI*) software.

The fast Fourier transform (FFT) of the acquired HRTEM images was computed. For any crystalline material, the FFT exhibits spots, whose position in reciprocal space is related to the orientation and spacing of lattice planes in real space.

EDXS and EELS were performed in the STEM mode by means of an electron probe of about 1–2 nm in diameter. Direct positioning of the electron beam on a nanometer-sized feature was, however, not accurate. A few-nm discrepancy could be observed between the set position and the position effectively measured by the electron beam. The most useful results were obtained by means of line scans: series of measurements are consecutively performed along a predefined line on the specimen. Here also, a discrepancy could be stated between the set positions and the measured positions. However, the discrepancy was systematic during one and the same line scan, so that the relative positioning of the electron beam during the scan – *i.e.* the distance between two consecutive measurements – was quite precise, allowing to probe the presence of an element on a nanometer scale. In addition, line scans are particularly interesting for the investigation of a sharp edge: even if the absolute positioning of the beam is not perfect, the edge may be hit at a certain moment of a line scan. Furthermore, the HAADF signal can be measured simultaneously to EDX or EEL spectra, giving a further indication on the exact location of the electron beam during the scan.

The EELS spectra were acquired with convergence and collection semi-angles of about 16 mrad and 13 mrad respectively. The energy resolution amounted to approximately 1.8 eV. When indicated, the EEL spectra were corrected for background as follow. The background was fitted within an energy window positioned immediately before the edge of interest and extrapolated beyond the edge onset. A power-law function was used for that purpose [29]. The extrapolated background was then subtracted from the edge.

3 Results and discussion

3.1 Localization of the neptunium

The first aim of the TEM analyses is determining the exact location where GR immobilizes Np. Figure 1 shows conventional bright-field TEM images of GR and Np-GR particles. It can be noted that the exposition of the GR particles to air and the possible dehydration (*cf*. Sect. 2.1) did not affect their characteristic hexagonal morphology. A few nm-wide dark rim is observed at the edge of the Np-GR platelets (Figure 1b), whereas such a rim is not visible for GR standard (Figure 1a).

Figure 2 shows a HAADF-STEM of Np-GR. On this image, the superposition of multiple platelets appears brighter and brighter as the total thickness probed by the electron beam increases. However, at constant thickness, the HAADF contrast is directly related to the atomic num-
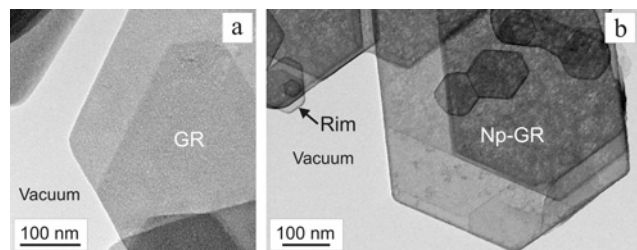

Fig. 1: Bright-field TEM images of GR standard (a) and Np-GR (b).
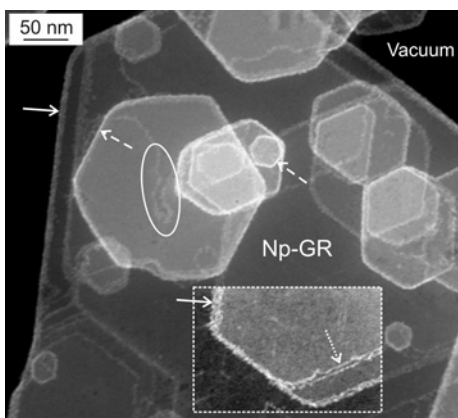
Fig. 2: HAADF-STEM image of Np-GR. In the insert, the contrast was digitally changed with respect to the rest of the image, in order to allow a better visualization of the rim.

Fig. 3: EDX line scan across the edge of Np-GR. a) HAADF-STEM image, the line marks the 32 nm path along which 16 spectra were recorded. b) HAADF signal as a function of the position of the electron probe during the line scan. c) EDX spectra representative for the vacuum region (1), the rim (2), and the inside of Np-GR (3). The Cu signal results from the TEM grid.

ber Z [*e.g.*, 30]. Thus, the rim, which appears in that case bright around the Np-GR platelets, suggests the presence of a high-Z element like neptunium.

The rim appears sometimes quite diffuse, for instance at the positions indicated by solid-line arrows in Fig. 2, with a width up to 15 nm and a moderate HAADF brightness. However, it appears much sharper at other positions as pointed out by the dashed-line arrows in Fig. 2, with a higher brightness and a width of only about 2.5–3 nm. Also, two distinct sharp parallel rims are observed at the position indicated by a dotted-line arrow (Figure 2). Hence, it suggests that at the "diffuse positions", the edges of the green-rust sheets are not perfectly superposed in the direction of the electron beam, leading to terraces that might be only few monolayers high but are surrounded by their own sharp rim. Some irregular chains or networks are also sometimes observable, *e.g.* at the position marked by an oval in Figure 2. They could correspond to an alteration of the shape of certain green-rust sheets, or to rim-constituting particles left behind by some Np-GR platelets removed during the specimen preparation.

To accurately correlate the high HAADF signal with the presence of Np, EDXS was performed by an electron probe of about 1–2 nm in diameter. Fig. 3 presents the results of a line scan performed across the rim with 16 spectra recorded on a 32 nm path (line in Figure 3a). The intensity of the HAADF signal is shown in Figure 3b as a function of the position of the electron probe during the scan. Three representative spectra are shown in Figure 3c. In spite of the imperfection of the absolute positioning of the electron beam (*cf.* Sect. 2.2), the rim of interest was hit during the line scan (point 2 in Figure 3b, corresponding to spectrum 2 in Figure 3c). A strong Np signal dominates the spectrum recorded at the rim (spectrum 2). In addition, Np
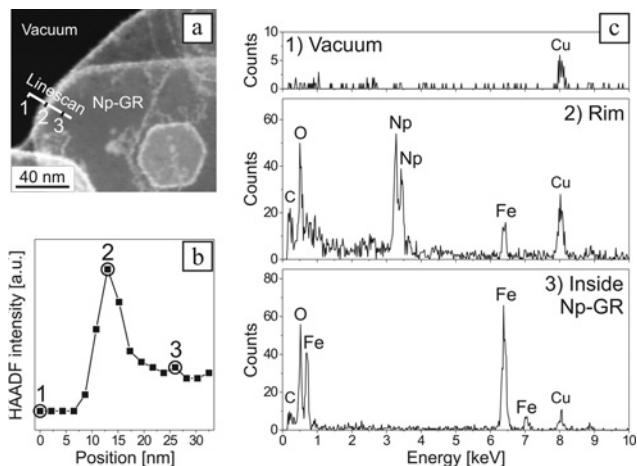
cannot be detected inside the GR particle (spectrum 3 in Figure 3c). The spectrum 3 representative for the inside of Np-GR was recorded only approximately 13 nm away from the spectrum 2 exhibiting the highest Np signal (*cf.* Figure 3b). Hence, Np is clearly localized at the edge of the GR platelets. Thus, the high spatial resolution achieved in the present work allows to confirm and to extend the observations of Christiansen *et al.* [22], who performed EDXS on comparable Np-GR particles. The authors concluded that Np is found enriched at the green-rust edges.

In addition, the results shown in Figure 3 clearly demonstrate the correlation between the strong HAADF signal (Point 2 in Figure 3b) and the presence of Np (spectrum 2 in Figure 3c). It illustrates the power of HAADF-STEM for the imaging of high-*Z* actinides, as pointed out by Utsunomiya *et al.* [30]. The method is especially efficient when actinide nanomaterials are enclosed in a heterogeneous system with other materials composed of lighter elements. In the present case, it allows a direct visualization of the nm-sized Np-rich regions with a strong contrast with respect to green rust (Figs. 3a and 3b).

3.2 Characterization of the Np-containing phase

XPS analyses showed that the interaction between NpO_2^+ and GR results in the reduction of Np(V) to Np(IV) [21, 22]. The second aim of the TEM analyses is to gather more information concerning the Np(IV)-containing phase formed.

This phase could be a Np dioxide or a Np-substituted iron oxide mineral. Indeed, O and Fe signals are also present in the EDX spectrum recorded at the edge (spectrum 2 in Figure 3c). However, a Cu signal is also measured in all the spectra, even in the one representative for the vacuum region (spectrum 1 in Figure 3c). It is an artifact resulting from the Cu TEM grid (Cu is the predominant element in the TEM specimen). As a matter of fact, not all of the X-rays measured by EDXS come from the region of interest where the primary electron beam is focused [e.g., 23]. Thus, it can be noted that the Cu peak is stronger at the Np-containing rim (spectrum 2 in Figure 3c) than inside the green rust (spectrum 3) or in the vacuum (spectrum 1). Indeed, Np is a strong electron scatterer (cf., e.g., the strong HAADF signal in Figure 3b), so that a high amount of scattered electrons may hit other parts of the specimen, e.g. the Cu grid bars or the C-film, generating X-rays. Hence, "spurious" Cu and C peaks are particularly intense in spectrum 2. Since Fe in the green rust is also present in high amount in the immediate vicinity of the primary electron beam, it is possible that a part of the Fe signal recorded in spectrum 2 results from such an artifact.

In contrast to EDXS, EELS, which measures forward transmitted electrons, is not affected by such an effect. Two EEL spectra of the inside and the rim of a Np-GR platelet, acquired under the same experimental conditions during one and the same line scan, are shown in Figure 4. The spectrum acquired inside the platelet is characterized by strong Fe-$M_{2,3}$ edges. At the rim, Np-$O_{4,5}$ edges appear at around 100 eV, whereas the intensity for the Fe edges almost completely vanishes (the intensity under the Fe edges is reduced by a factor of more than 15 with respect to the spectrum taken inside Np-GR). In addition, the positioning of the electron beam on the rim is not particularly accurate (cf. Sect. 2.2) and the edges of the green-rust sheets may be imperfectly superposed in the direction of the electron beam (cf. Sect. 3.1). Hence, the residual Fe signal at the rim likely comes from the electron beam pass-
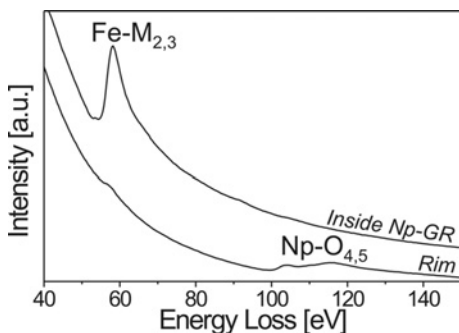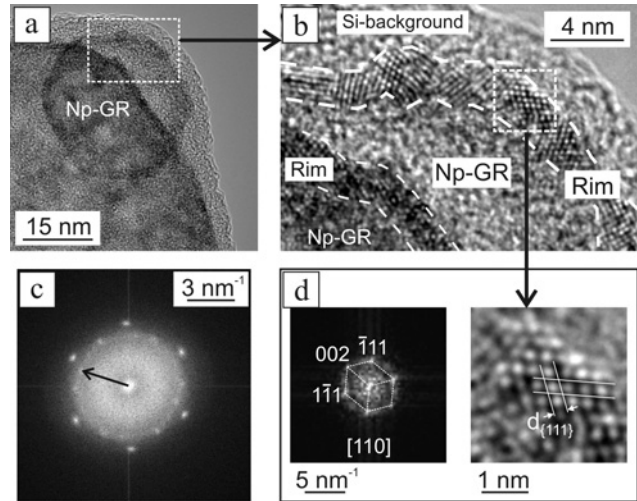

Fig. 5: HRTEM of Np-GR. a) HRTEM image. b) Detail of (a). The Si-containing background results from a contamination. c) FFT of an HRTEM image (same specimen region as shown in (a), but slightly different focus conditions). The arrow indicates the position of a spot resulting from the rim with respect to the center of the FFT. d) Detail of the rim. The lattice-fringe pattern and the corresponding FFT are consistent with [110]-oriented NpO_2 (fluorite-type structure).

ing through the Np-containing rim and hitting some underlying or adjacent GR region, resulting in the weak signal (a part of the Fe signal recorded in the EDX spectrum 2 of Figure 3c likely has a similar origin). Thus, the EELS results strongly suggest that Fe is not present at the rim together with Np in one and the same phase, i.e. that the rim does not consist of a Np-substituted iron oxide phase.

HRTEM provides further insight into the Np-phase at the rim. The observed lattice-fringe patterns indicate that the rim is composed of nanocrystallites about 2–3.5 nm in size. Figure 5a,b shows, for example, two distinct Np-GR platelets and their associated rims comprised of nanocrystallites. The platelets are superposed on an amorphous contamination film stemming from the specimen holder. Nevertheless, this thin amorphous background does not inhibit measurement of the Np-GR lattice-fringe patterns.

When the intense electron beam is focused on the GR platelets to perform HRTEM, some radiation damage occurs. A HRTEM image of GR standard was recorded as quickly as possible after the HRTEM beam conditions were set and its FFT is shown in Figure 6a. The same GR specimen region was exposed to the HRTEM beam conditions for about ten more minutes. As a result, several new spots appear in the FFT (Figure 6b) compared to the initial FFT (Figure 6a), indicating a beam-induced reorganization of the atoms in the crystal structure. The same effect was observed investigating Np-GR. Complete understanding of this phenomenon is beyond the scope of the present work.
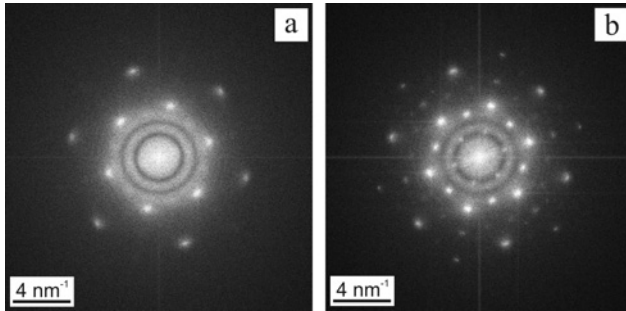

Fig. 4: EEL spectra taken "inside" a Np-GR platelet and at its rim.

Fig. 6: FFTs of HRTEM images of GR standard. a) Immediately after the HRTEM beam conditions were set; b) about ten minutes later.

However it is necessary to include this effect when analyzing the HRTEM images of Np-GR. That way, some additional spots can be identified in the FFTs, which clearly originate from the Np-containing nanocrystallites at the rim, and not from beam-damaged GR. In contrast to the GR platelets, the rim was not observed to exhibit beam damage during the HRTEM experiments.

The position of some spots corresponding to the rim is measured with respect to the center of the FFT (see Figure 5c). FFTs of different images gave an average lattice-plane spacing d of about 3.14 ± 0.05 Å (the given precision corresponds to $\pm\sigma$, with σ the standard deviation determined from 18 measurements of d). This value is in very good agreement with the d-spacing of 3.1370 Å determined from crystallographic data [31] for the {111} crystal-plane spacing in NpO_2. In addition, the measured spots are the nearest from the center of the FFT that can be attributed to the nanocrystallites. This aspect is also in accordance with NpO_2 and its fcc fluorite-type structure (*Fm3m* space group), where the {111} crystal planes are the planes of highest d-spacing expected in the FFT.

The selection of only a small part of an HRTEM image for FFT calculations results in a FFT of lower definition, and thus limits the reliability of d-spacing measurements. However, by selecting only particular details of the rim, the influence of the signal induced by the inside of Np-GR becomes negligible. That way, a further family of rim-specific spots can be identified, confirming the fluorite-type structure of NpO_2. Other d-spacing values of about 2.7 Å or 2.8 Å are found (results from five measurements), which are in good agreement with the nominal value $d \sim 2.7167$ Å expected for the {002} crystal planes of NpO_2 (d-value calculated from Fahey *et al.* [31]. Figure 5d exhibits a detail of the rim. The observed lattice-fringe pattern and the corresponding FFT are consistent with the NpO_2 structure in the [110] orientation. Recently, Powell *et al.* [32] investigated [110]-oriented PuO_2 nano-colloids by HRTEM. PuO_2 and NpO_2 are isostructural (fcc fluorite-type structure, *Fm3m*

space group). As a result, the HRTEM data for the [110] zone axis are very similar.

3.3 EELS of neptunium dioxide

Up to now, only a few published studies involved EELS to investigate Np-containing materials. In addition, most of the data available in the literature concern the investigation of the elemental metal α-Np in the frame of larger studies of the electronic and magnetic structure of actinide metals by means of the $O_{4,5}$ and $N_{4,5}$ edges [33–37], or the detection of low levels of Np in uranium-bearing solids using principally the $M_{4,5}$ edges [38–44]. Buck *et al.* [44] analyzed the Np-$M_{4,5}$ edges of a NpO_2 standard in a study correlating the actinide M_4/M_5 intensity ratios with the number of 5f electrons, but they did not publish the corresponding EEL reference spectrum. Hence, a comprehensive set of EELS reference data for Np materials of known phases is still missing. However, such data would be a prerequisite for the accurate EELS investigation of an unknown Np compound.

Furthermore, EEL spectra are to some extent similar to X-ray absorption spectroscopy (XAS) data [45]. In the present work, the Np-$O_{4,5}$ edges were recorded by EELS, whereas, to our knowledge, no XAS data were published up to now for the Np-$O_{4,5}$ edges.

The EEL spectrum recorded at the rim of Np-GR (Figure 4) is shown in Figure 7 after subtraction of the background under the Np-$O_{4,5}$ edges. Altogether, the previous results from XPS [22], EELS, and more particularly HRTEM (this study) exhibit that the rim is composed of crystalline
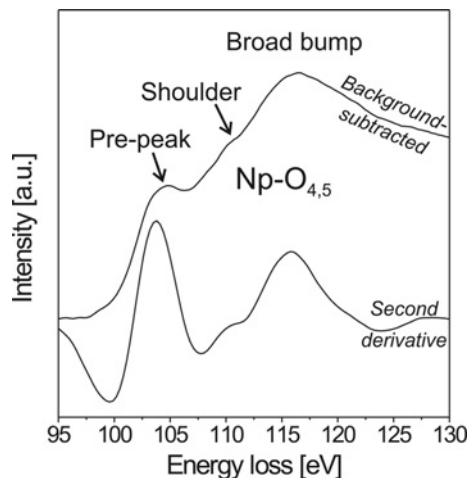

Fig. 7: EEL spectrum recorded at the rim of Np-GR (*cf.* Figure 4): Np-$O_{4,5}$ edges after background subtraction, and after subsequent calculation of the second derivative.

NpO$_2$. Hence, it is the first time that the Np-O$_{4,5}$ EEL spectrum is presented for NpO$_2$, or more generally for a Np(IV) phase.

The Np-O$_{4,5}$ edges are mainly attributed to the transition of Np 5d electrons to unoccupied 5f states. The spectrum is characterized by a sharp pre-peak followed by a broader second bump (Figure 7). The splitting between the two peaks is approximately 12 eV. In addition, a shoulder is observable on the lower-energy side of the broad bump. The second derivative of the Np-O$_{4,5}$ spectrum is also shown in Figure 7. It improves the visibility of the shoulder by enhancing fast varying features and removing non-varying features [43]. The splitting between the shoulder and the peak of the bump is about 5–6 eV. The specimen position where the spectrum was taken was slightly contaminated by a Si-containing compound. The onset of the Si-L$_{2,3}$ edges is at about 99 eV, which could perturb the measurement of the Np-O$_{4,5}$ edges. However, the Si signal is very weak compared to the Np signal and is hardly visible on the raw spectrum taken inside Np-GR (Figure 4, no pronounced signal around 100 eV). As a test, the weak Si signal measured inside GR was subtracted from the EEL signal measured at the rim. It did not affect the observed structure of the Np-O$_{4,5}$ edges, exhibiting that the Si signal can be neglected.

To date, uranium is the actinide that has been investigated most by means of EELS. A structure similar to that obtained in the present work for Np-O$_{4,5}$ (sharp pre-peak and broad second peak) was reported by Moore and van der Laan [33] for the U-O$_{4,5}$ edges of U metal and UO$_2$. The authors also presented the second derivative of the EEL spectra, and whereas a shoulder was hardly recognizable on the lower-energy side of the broad peak for U, a pronounced shoulder was visible for UO$_2$, exhibiting that the shoulder is sensitive to the bonding environment. Rice *et al.* [46] investigated the U-O$_{4,5}$ edges for different uranium oxides and fluorides and suggested that the shoulder allows the distinction between different oxidation states: where a shoulder was observed for the compounds having uranium in the 4+ state (UO$_2$, UF$_4$), the uranium 6+ compounds (UO$_3$, UO$_2$F$_2$) did not exhibit this feature (however, no second derivative was calculated). Hence, the shoulder should be considered as a feature characteristic for the oxidation state rather than a phase-specific property. Butterfield *et al.* [37] presented the O$_{4,5}$ EEL spectra for different actinide elemental metals, including α-Np. The Np-O$_{4,5}$ spectrum was also found to consist of a pre-peak followed by a broader second peak. Nevertheless, it is difficult to distinguish a shoulder on the second peak of the spectrum published for α-Np [37] (the second derivative, however, was not calculated), whereas a shoulder is clearly

visible in the present work, even on the original spectrum obtained without second derivative (Figure 7). Hence, the pronounced shoulder measured in the present work on the Np-O$_{4,5}$ edges (Figure 7) – similar to that observed for UO$_2$ by Moore and van der Laan [33] – once again appears consistent with NpO$_2$.

Moore and van der Laan [33] and Butterfield *et al.* [37] also showed that both the O$_4$ and O$_5$ peaks are in fact encapsulated in the broad second bump, whereas the sharp pre-peak corresponds to a dipole-"forbidden" transition induced by the finite spin-orbit interaction. Hence, the shoulder in Figure 7 could be considered as a manifestation of the Np-O$_5$ peak (5d$_{5/2}$ $\rightarrow$ 5f transition) and the peak of the bump mainly attributed to Np-O$_4$ (5d$_{3/2}$ $\rightarrow$ 5f transition).

3.4 Immobilization process and outlook

In the present work, the term "immobilization" refers to the removal of the Np(V) from the aqueous solution and its incorporation as Np(IV) into a solid phase. This way the otherwise high mobility of the neptunyl ions is lowered. However, the decrease of the mobility does not mean that the transport of Np in the environment would stop completely even if it is bound to GR. Indeed, GR and the nanoparticles attached to it could still be transported as colloids along the water flow path. In addition, Np could be released later as a function of the environmental conditions. This last problem was partly addressed by Christiansen *et al.* [22] who reported encouraging results. They showed that a major part of the Np attached to GR remains incorporated, in its tetravalent form, into a solid phase, even if the redox conditions turn from reducing to oxidizing. In any case, it is clear that GR can attenuate the migration of Np.

The HAADF-STEM, HRTEM, EDXS and EELS investigations exhibit the preferential immobilization of Np at the edge of the Np-GR particles and confirm the previous observations by Skovbjerg *et al.* [21] and Christiansen *et al.* [22]. There is, thus, no evidence for neptunyl entry into the GR interlayers. If the neptunyl ions have access to the interlayer space (about 9 Å thick, [21]), they do not seem to be able to be trapped there by incorporation. Different types of GR exist, varying in their interlayer anion and consequently in the interlayer thickness. For instance, beside GR sulphate, carbonate and chloride forms occur in nature [7, 47, 48]. Previous studies have shown that the ability of a given species to be incorporated in the GR interlayer depends on its charge, size, and geometry with respect to the interlayer thickness and anion type [19, 21]. For instance, the tetrahedral chromate anion (CrO$_4^{2-}$) is similar in charge,

size, and geometry to sulphate (SO_4^{2-}) and was found to be incorporated into the $GR_{Na,SO4}$ interlayer. In contrast the neptunyl ion (NpO_2^+) is positively charged and linear. Hence, it is not surprising if the ability of these species to substitute into the GR-sulphate structure is restricted. Indeed, O'Loughlin et al. [15] investigated the reduction of uranyl (UO_2^{2+}, linear) by GR_{SO4} and also reported the immobilization of U(IV) at the edge of the GR in the form of UO_2 nanoparticles. Hence, in spite of slightly different charges, uranyl and neptunyl cations behave quite similarly with respect to GR_{SO4}. In the present study, Na^+ cations are also associated into the interlayer structure ($GR_{Na,SO4}$). Nevertheless, the fact that Na^+ and NpO_2^+ have the same charge does not seem to be a sufficient condition for NpO_2^+ to be able to substitute for Na^+ in the GR interlayer, because these cations strongly differ in size and geometry.

A priori, the location of the Np at the Np-GR edges tends to indicate that in the present case the high surface area and the layered structure of $GR_{Na,SO4}$ do not play a decisive role in its high reactivity. Nevertheless, Wander et al. [49] demonstrated that charge transport is facile along the hydroxyl layers. Hence, the layered structure may favor charge transfer being a sub-step of neptunyl reduction at the edge.

Thus, the preferential immobilization of Np at the rim suggests the fast sorption within 10 min of the neptunyl ions at the GR edge followed by their reduction and the subsequent growth of NpO_2 nanoparticles [22]. However, there might be other possible mechanisms. Indeed, some of the neptunyl could be reduced by aqueous Fe(II) in the supernatant. Neck et al. [25] studied the reduction of Np(V) to Np(IV) in aqueous solutions and described the formation of colloidal hydrated NpO_2 particles. Following the interpretation that Neck et al. [25] made of their results, at least three competing processes could be envisaged of how the observed Np-containing rim could be generated:

1. Initial sorption of the neptunyl at the GR edge, then reduction, finally growth of NpO_2 nanoparticles.
2. Initial reduction of the neptunyl in the aqueous solution, and sorption of the formed Np(IV) species at the GR edge, finally growth of NpO_2 nanoparticles.
3. Initial reduction of the neptunyl in the aqueous solution, then agglomeration of the formed Np(IV) species into NpO_2 nanoparticles, finally sorption of the nanoparticles at the GR edge.

Under these pH and pe conditions (pH ∼ 8, pe ∼ −6.7), the predominance of species $Np(OH)_4$(aq) in the aqueous phase is predicted according to thermodynamic data reported in the NEA-TDB [50]. The second process seems to be unlikely, as reduction in homogenous solution will result in uncharged $Np(OH)_4$(aq) species which may not preferentially adsorb at the edges of GR. In addition, homogeneous reduction of Np(V) by Fe(II) ions is much slower than in presence of of a Fe(II) bearing solid as observed by Nakata et al. [51] at pH 5.7 to 5.9 and magnetite. By discussing how the GR basal planes, the GR edges, and colloidal NpO_2 are charged, Christiansen et al. [22] concluded that if NpO_2 nanoparticles were formed by homogeneous reduction and precipitation from solution (process 3), i.e. polymerisation of $Np(OH)_4$(aq) species and condensation of OH bonds, their preferential attachment at the GR edge would be unexpected.

In the present work, the GR edges are systematically decorated by a dense and continuous rim (Figs. 1b, 2, 3a, and 5a,b). Single nanoparticles are hardly recognizable. After the reduction of UO_2^{2+} by GR_{SO4}, O'Loughlin et al. [15] clearly observed discrete UO_2 particles (∼ 2–9 nm in diameter) by dark-field TEM imaging: by selecting only specific diffracted beams to contribute to the image, some crystallites might not be visible in the image, which emphasizes the adequately oriented particles. This is not the case for the TEM bright field, HRTEM, and HAADF STEM images shown in the present work (Figures 1b, 2, 3a, and 5a,b). These TEM images are projections in two dimensions of the three dimensional specimen regions. Some particles which appear to touch each other might in fact not be in direct contact which each other, but only partly overlaid in the direction of the electron beam. However, the fact that the rim appears systematically continuous and dense on the images strongly suggests that the constituting nanoparticles effectively are closely packed. This constant and tight arrangement of the nanocrystallites appears more consistent with a growth of the NpO_2 solid directly at the GR edges (after the sorption step, processes 1 or 2), than with the initial formation of the NpO_2 nanoparticles in the solution and subsequent deposition at the edge (process 3).

The reduction of Np(V) to Np(IV) by green rust implies the simultaneous oxidation of Fe(II) to Fe(III). Earlier inspections by using XPS could not recognize such variation in Fe(II)/Fe(III) ratio upon Np(V) reduction [22]. Possible reasons are the relatively low Np(V):Fe(II)$_{GR}$ molar ratio (∼ 7 : 100). Notably if we assume eventual charge transfer between the center and the edge of the GR particle or additional incorporation of Fe^{2+}(aq) to compensate for the oxidation of Fe(II) in the green rust structure, the identification of partial Fe(II) oxidation will be very challenging. Furthermore, Np-induced Fe(II) oxidation might be masked by partial oxidation during sample transfer (see discussion in the experimental section). A proper investigation of this important topic by TEM or spectromicro-

scopic methods implies an anoxic transfer of the specimen between the preparation glove-box and the vacuum of the microscope, a thorough understanding of beam damage, and ideally the use of a technique to monitor the Fe(II)/Fe(III) ratio within the GR platelets, *e.g.* based on EELS [*e.g.*, 52, 53] in samples containing a higher Np/Fe ratio.

4 Conclusion

In the present study, green rust in sodium sulphate form was reacted with an aqueous solution of neptunyl ions (NpO_2^+), resulting in the formation of a Np(IV) solid phase. TEM investigations at nanometer scale showed that the neptunium is immobilized at the edge of green rust platelets, in a rim composed of nanocrystallites about 2–3.5 nm in size. Findings of EELS and HRTEM of these nanocrystallites are consistent with NpO_2. Thus, in presence of green rust, Np(V) is effectively removed from aqueous solution by reduction and formation of less soluble tetravalent Np oxide, demonstrating one possible immobilization mechanism for Np(V) in the context of deep geological nuclear-waste disposal. Hence, green rust is a promising material for attenuating the environmental migration of redox-sensitive waste-born radionuclides like Np.

To complete the understanding of the immobilization mechanism, further research will have to determine the nature of the Fe(III)-rich material that is expected to be formed as a counterpart to the reduction of Np(V). Furthermore, GR sodium sulphate might be present in sulphate rich groundwater and in marine influenced environments, but carbonate green rust, is the predominant form of GR expected in the nature (*e.g.* in groundwater, [7]). Also GR chloride could form in the vicinity of corroding steel [54] and in water with high salinity. Hence, a systematic study of the interaction between radionuclide species, *e.g.* neptunyl, and GR of different forms should be made for the prediction of the environmental migration of radionuclides released from a nuclear-waste repository after water ingress.

References

1. Ewing, R. C., Runde, W., Albrecht-Schmitt, T. E.: Environmental impact of the nuclear fuel cycle: fate of actinides. MRS Bull. **35**, 859 (2010).

2. Kaszuba, J. P., Runde, W. H.: The aqueous geochemistry of neptunium: dynamic control of soluble concentrations with applications to nuclear waste disposal. Environ. Sci. Technol. **33**, 4427 (1999).

3. Refait, P., Abdelmoula, M., Génin, J.-M.R.: Mechanisms of formation and structure of green rust one in aqueous corrosion of iron in the presence of chloride ions. Corros. Sci. **40**, 1547 (1998).

4. Géhin, A., Ruby, C., Abdelmoula, M., Benali, O., Ghanbaja, J., Refait, P., Génin, J.-M.R.: Synthesis of Fe(II-III) hydroxysulphate green rust by coprecipitation. Solid State Sci. **4**, 61 (2002).

5. Simon, L., Francois, M., Refait, P., Renaudin, G., Lelaurain, M., Génin, J.-M.R.: Structure of the Fe(II-III) layered double hydroxysulphate green rust two from Rietveld analysis. Solid State Sci. **5**, 327 (2003).

6. Christiansen, B. C., Balic-Zunic, T., Petit, P. O., Frandsen, C., Morup, S., Geckeis, H., Katerinopoulou, A., Stipp, S. L. S.: Composition and structure of an iron-bearing, layered double hydroxide (LDH) – green rust sodium sulphate. Geochim. Cosmochim. Acta **73**, 3579 (2009).

7. Christiansen, B. C., Balic-Zunic, T., Dideriksen, K., Stipp, S. L. S.: Identification of green rust in groundwater. Environ. Sci. Technol. **43**, 3436 (2009).

8. Gu, B., Phelps, T. J., Liang, L., Dickey, M. J., Roh, Y., Kinsall, B. L., Palumbo, A. V., Jacobs, G. K.: Biogeochemical dynamics in zero-valent iron columns: Implications for permeable reactive barriers. Environ. Sci. Technol. **33**, 2170 (1999).

9. Roh, Y., Lee, S. Y., Elless, M. P.: Characterization of corrosion products in the permeable reactive barriers. Environ. Geol. **40**, 184 (2000).

10. Wilkin, R. T., Su, C., Ford, R. G., Paul, C. J.: Chromium-removal processes during groundwater remediation by a zerovalent iron permeable reactive barrier. Environ. Sci. Technol. **39**, 4599 (2005).

11. Loyaux-Lawniczak, S., Refait, P., Ehrhardt, J.-J., Lecomte, P., Génin, J.-M.R.: Trapping of Cr by formation of ferrihydrite during the reduction of chromate ions by Fe(II)-Fe(III) hydroxysalt green rusts. Environ. Sci. Technol. **34**, 438 (2000).

12. Refait, P., Simon, L., Génin, J.-M.R.: Reduction of SeO_4^{2-} anions and anoxic formation of iron(II)-iron(III) hydroxyl-selenate green rust. Environ. Sci. Technol. **34**, 819 (2000).

13. Dodge, C. J., Francis, A. J., Gillow, J. B., Halada, G. P., Eng, C., Clayton, C. R.: Association of uranium with iron oxides typically formed on corroding steel surfaces. Environ. Sci. Technol. **36**, 3504 (2002).

14. Bond, D. L., Fendorf, S.: Kinetics and structural constraints of chromate reduction by green rusts. Environ. Sci. Technol. **37**, 2750 (2003).

15. O'Loughlin, E. J., Kelly, S. D., Cook, R. E., Csencsits, R., Kemner, K. M.: Reduction of uranium(VI) by mixed iron(II)/iron(III) hydroxide (green rust): Formation of UO_2 nanoparticles. Environ. Sci. Technol. **37**, 721 (2003).

16. O'Loughlin, E. J., Kelly, S. D., Kemner, K. M., Csencsits, R., Cook, R. E.: Reduction of Ag^I, Au^{III}, Cu^{II}, and Hg^{II} by Fe^{II}/Fe^{III} hydroxysulfate green rust. Chemosphere **53**, 437 (2003).

17. Pepper, S. E., Bunker, D. J., Bryan, N. D., Livens, F. R., Charnock, J. M., Pattrick, R. A. D., Collison, D.: Treatment of radioactive wastes: An X-ray absorption spectroscopy study of the reaction of technetium with green rust. J. Colloid Interface Sci. **268**, 408 (2003).

18. Legrand, L., Figuigui, A. E., Mercier, F., Chaussé, A.: Reduction of aqueous chromate by Fe(II)/Fe(III) carbonate green rust: Kinetic and mechanistic Studies. Environ. Sci. Technol. **38**, 4587 (2004).

19. Skovbjerg, L. L., Stipp, S. L. S., Utsunomiya, S., Ewing, R. C.: The mechanisms of reduction of hexavalent chromium by green rust sodium sulphate: Formation of Cr-goethite. Geochim. Cosmochim. Acta **70**, 3582 (2006).

20. Hayashi, H., Kanie, K., Shinoda, K., Muramatsu, A., Suzuki, S., Sasaki, H.: pH-dependence of selenate removal from liquid phase by reductive Fe(II)-Fe(III) hydroxysulfate compound, green rust. Chemosphere **76**, 638 (2009).

21. Skovbjerg, L. L., Christiansen, B. C., Nedel, S., Dideriksen, K., Stipp, S. L. S.: The role of green rust in the migration of radionuclides: An overview of processes that can control mobility of radioactive elements in the environment using as examples Np, Se and Cr. Radiochim. Acta **98**, 607 (2010).

22. Christiansen, B. C., Geckeis, H., Marquardt, C. M., Bauer, A., Römer, J., Wiss, T., Schild, D., Stipp, S. L. S.: Neptunyl (NpO_2^+) interaction with green rust, $GR_{Na,SO4}$. Geochim. Cosmochim. Acta **75**, 1216 (2011).

23. Williams, D. B., Carter, C. B.: *Transmission Electron Microscopy*. 2nd ed., Springer, New York (2009).

24. Moore, K. T.: X-ray and electron microscopy of actinide materials. Micron **41**, 336 (2010).

25. Neck, V., Altmaier, M., Runke, J., Fellhauer, D., Lützenkirchen, J., Skerencak, A., Panak, P. J., Klenze, R., Fanghänel, T.: Chemistry and thermodynamic of actinides in aqueous solution. In: Geckeis, H. and Klenze, R. (Eds): FZK report, FZKA **7510**, 11 (2009) (electronically available from www.ine.kit.edu).

26. Paterson, J. H., Krivanek, O. L.: ELNES of 3d transition-metal oxides II. Variations with oxidation state and crystal structure. Ultramicroscopy **32**, 319 (1990).

27. Bach, D., Schneider, R., Gerthsen, D., Verbeeck, J., Sigle, W.: EELS of niobium and stoichiometric niobium-oxide phases. Part I: Plasmon and near-edges fine structure. Microsc. Microanal. **15**, 505 (2009).

28. Guilbaud, R., White, M. L., Poulton, S. W.: Surface charge and growth of sulphate and carbonate green rust in aqueous media. Geochim. Cosmochim. Acta **108**, 131 (2013).

29. Egerton, R. F.: *Electron Energy-Loss Spectroscopy in the Electron Microscope*. Plenum Press, New York (1986).

30. Utsunomiya, S., Kogawa, M., Kamiishi, E., Ewing, R. C.: Scanning transmission electron microscopy and related techniques for research on actinides and radionuclide nanomaterials. In: Kalmykov, S. N., Denecke, M. A. (Eds): *Actinide Nanoparticle Research*. Springer Verlag, Heidelberg (2011), p. 33.

31. Fahey, J. A., Turcotte, R. P., Chikalla, T. D.: Decomposition, stoichiometry and structure of neptunium oxides. J. Inorg. Nucl. Chem. **38**, 495 (1976).

32. Powell, B. A., Dai, Z., Zavarin, M., Zhao, P., Kersting, A. B.: Stabilization of plutonium nano-colloids by epitaxial distortion on mineral surfaces. Environ. Sci. Technol. **45**, 2698 (2011).

33. Moore, K. T., van der Laan, G.: Accurate labeling of the light-actinide $O_{4,5}$ edges. Ultramicroscopy **107**, 1201 (2007).

34. Moore, K. T., van der Laan, G., Wall, M. A., Schwartz, A. J., Haire, R. G.: Rampant changes in $5f_{5/2}$ and $5f_{7/2}$ filling across the light and middle actinide metals: electron energy-loss spectroscopy, many-electron atomic spectral calculations, and spin-orbit sum rule. Phys. Rev. B **76**, 073105 (2007).

35. Moore, K. T., van der Laan, G.: Nature of the 5f states in actinide metals. Rev. Mod. Phys. **81**, 235 (2009).

36. van der Laan, G., Moore, K. T.: Spin-Orbit coupling *vs.* exchange interaction in actinide metals. Mater. Res. Soc. Symp. Proc. **1104**, 153 (2008).

37. Butterfield, M. T., Moore, K. T., van der Laan, G., Wall, M. A., Haire, R. G.: Understanding the $O_{4,5}$ edge structure of actinide metals: electron energy-loss spectroscopy and atomic spectral calculations of Th, U, Np, Pu, Am, and Cm. Phys. Rev. B **77**, 113109 (2008).

38. Buck, E. C., Fortner, J. A.: Detecting low levels of transuranics with electron energy loss spectroscopy. Ultramicroscopy **67**, 69 (1997).

39. Finch, R. J., Fortner, J. A., Buck, E. C., Wolf, S. F.: Neptunium incorporation into uranium(VI) compounds formed during aqueous corrosion of neptunium-bearing uranium oxides. Mater. Res. Soc. Symp. Proc. **713**, 647 (2002).

40. Fortner, J. A., Finch, R. J., Kropf, A. J., Cunnane, J. C.: Re-evaluating neptunium in uranyl phases derived from corroded spent fuel. Nucl. Technol. **148**, 174 (2004).

41. Buck, E. C., Hanson, B. D., Friese, J. I., Douglas, M., McNamara, B. K.: Evidence for neptunium incorporation into uranium(VI) phases. Mater. Res. Soc. Symp. Proc. **824**, 133 (2004).

42. Douglas, M., Clark, S. B., Friese, J. I., Arey, B. W., Buck, E. C., Hanson, B. D., Utsunomiya, S., Ewing, R. C.: Microscale characterization of uranium(VI) silicate solids and associated neptunium(V). Radiochim. Acta **93**, 265 (2005).

43. Buck, E. C., Douglas, M., Wittman, R. S.: Verifying the presence of low levels of neptunium in a uranium matrix with electron energy-loss spectroscopy. Micron **41**, 65 (2010).

44. Buck, E. C., Finn, P. A., Bates, J. K.: Electron energy-loss spectroscopy of anomalous plutonium behavior in nuclear waste materials. Micron **35**, 235 (2004).

45. Moore, K. T., Wall, M. A., Schwartz, A. J., Chung, B. W., Morton, S. A., Tobin, J. G., Lazar, S., Tichelaar, F. D., Zandbergen, H. W., Söderlind, P., van der Laan, G.: Electron-energy-loss spectroscopy and X-ray absorption spectroscopy as complementary probes for complex f-electron metals: cerium and plutonium. Philos. Mag. **84**, 1039 (2004).

46. Rice, S. B., Bales, H. H., Roth, J. R., Whiteside, A. L.: Empirical identification of uranium oxides and fluorides using electron energy-loss spectroscopy in the transmission electron microscope. Microsc. Microanal. **5**, 437 (1999).

47. Bearcock, J. M., Perkins, W. T., Dinelli, E., Wade, S. C.: Fe(II)/Fe(III) 'green rust' developed within ochreous coal mine drainage sediment in South Wales, UK. Mineral. Mag. **70**(6), 731 (2006).

48. Génin, J.-M. R., Bourrié, G., Trolard, F., Abdelmoula, M., Jaffrezic, A., Refait, P., Maitre, V., Humbert, B., Herbillion, A.: Thermodynamic equilibria in aqueous suspensions of synthetic and natural Fe(II)-Fe(III) green rusts: occurrences of the mineral in hydromorphic soils. Environ. Sci. Technol. **32**, 1058 (1998).

49. Wander, M. C. F., Rosso, K. M., Schoonen, M. A. A.: Structure and charge hopping dynamics in green rust. J. Phys. Chem. C **111**, 11414 (2007).

50. Guillaumont, R., Fanghänel, T., Neck, V., Fuger, J., Palmer, D. A., Grenthe, I., Rand, M. H.: *Chemical Thermodynamics 5, Update on the Chemical Termodynamics of Uranium, Neptunium, Plutonium, Americium and Technetium.* (Eds.: Mompean, F. J., Illemassene, M., Domenech-Orti, C., Ben Said, K.), OECD-NEA Data Bank, Issy-les-Moulineaux, France, Elsevier, Amsterdam, 293 (2003), ISBN: 0-444-51401-5.

51. Nakata, K., Nagasaki, S., Tanaka, S., Sakamoto, Y., Tanaka, T., Ogawa, H.: Reduction rate of neptunium(V) in heterogeneous solution with magnetite. Radiochim. Acta **92**, 145 (2004).

52. Garvie, L. A.J, Buseck, P. R.: Ratios of ferrous to ferric iron from nanometer-sized areas in minerals. Nature **396**, 667 (1998).

53. van Aken, P. A., Liebscher, B., Styrsa, V. J.: Quantitative determination of iron oxidation states in minerals using Fe $L_{2,3}$-edge electron energy-loss near-edge structure spectroscopy. Phys. Chem. Miner. **25**, 323 (1998).

54. Kounde, B., Raharinaivo, A., Olowe, A. A., Rezel, D., Bauer, P., Génin, J.-M.R.: Mössbauer characterization of the corrosion products of steel in civil works: Suspension bridge and reinforced concrete. Hyperfine Interactions **46**, 421 (1989).